Article

In-Depth Inhomogeneities in CIGS Solar Cells: Identifying Regions for Performance Limitations by PIXE and EBS

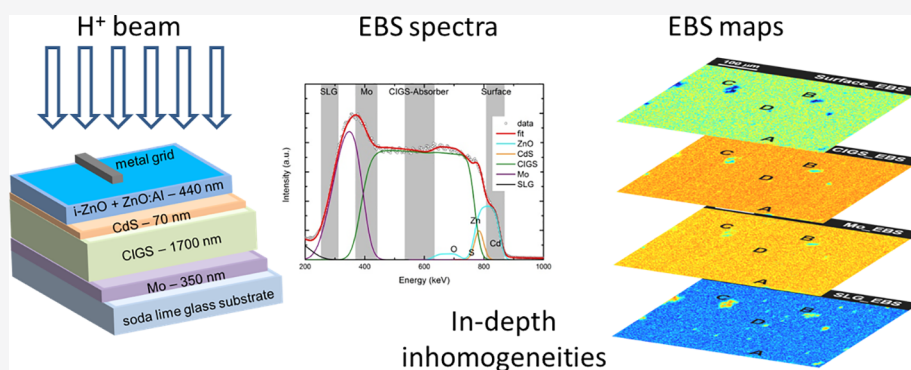Victoria Corregidor,* M. Alexandra Barreiros, Pedro M. P. Salomé, and Luís C. Alves

ACCESS | 📊 Metrics & More | 📰 Article Recommendations

ABSTRACT: When considering materials to be used as active layers in solar cells, an important required parameter is the proper knowledge of their elemental composition. It should be heavily controlled during growth in order to obtain the desired band gap and to decrease the recombination defects and then increase the solar cell electrical performance. Ion beam analytical (IBA) techniques and, in particular, particle-induced X-ray emission (PIXE) and elastic backscattering spectrometry (EBS) are quite suitable to determine the thickness and composition of such active layers. Furthermore, if these techniques are performed using a nuclear microprobe, lateral and in-depth inhomogeneities can be clearly observed from 2D maps. In many cases, composition variations can be detected from the classical 2D maps obtained from the PIXE spectra. In this work, it is shown how the in-depth variations can also be studied when considering 2D maps reconstructed from the EBS spectra. Such variations are derived from processing conditions and can be related to (i) composition, (ii) thickness, (iii) roughness, and (iv) other nontrivial issues. Examples obtained on Cu(In,Ga)Se$_2$-based cells are presented and discussed. Furthermore, the combination of IBA techniques such as PIXE and EBS is shown to be a competitive and alternative method to the more used and established techniques such as X-ray fluorescence for checking the average composition of the solar cell active layers or secondary ion mass spectroscopy for determination of the elemental depth profile.
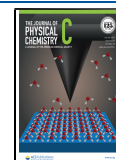
1. INTRODUCTION

Ion beam analytical (IBA) techniques, in particular, PIXE (particle-induced X-ray emission) and EBS (elastic back-scattering spectrometry), are commonly used for determining the elemental composition on a wide range of materials and devices.[1] PIXE enables to quantify a sample elemental concentration from the peak intensities of the characteristic X-ray emitted from the atoms during particle irradiation. PIXE is a very sensitive technique capable of providing information for elements of atomic number down to $Z = 11$,[2,3] and contrary to many other techniques, it does not require any calibration sample. EBS is quite sensitive to depth elemental profiling, allowing for sample in-depth composition determination by recording the backscattered ions' energy.[1] The major draw-backs of PIXE are that it does not provide depth resolved information, and there might be an overlap of the X-ray characteristic energy values. The major drawbacks of EBS are

the low sensitivity for light elements in a high Z matrix and, in some cases, the difficulty to distinguish elements with similar atomic number at different depths. Such disadvantages can be overcome by combining all obtained data during particle irradiation and performing a simultaneous analysis using the total IBA concept.[4] The data to be combined can be acquired using different experimental conditions (beam energy or beam particles) or other ion beam nuclear-based methods such as nuclear reaction analysis or elastic recoil detection analysis.

The IBA technique capabilities are enhanced when coupled to a scanning nuclear microprobe[5] due to (i) the possibility of focusing the beam to sub-micrometer spot sizes[6] (sometimes deep sub-micron[7]) and (ii) the possibility of rastering a specimen area under analysis to determine elemental distributions in one or two dimensions in a fully quantitative manner while adding imaging capabilities. Furthermore, the nuclear microprobes are usually equipped with both X-ray and particle detectors allowing for simultaneous acquisition of PIXE and EBS spectra, making it possible to perform the combined analysis of the collected data. See, for example, refs 8 and 9 where perovskite thin films were characterized using this procedure in order to get the depth compositional profile.

Nuclear microprobes also allow determining the interactions of macrostructured bioactive glasses with biological medium[10] or for 3D imaging and quantification of metal nanoparticles in light matrix specimens, such as biological cells. Chen et al.[11] obtained 3D high-resolution imaging on the distribution of gold nanoparticles inside a cell by using 1.6 MeV helium ions and combining scanning transmission ion microscopy, forward scattering transmission ion microscopy, and elastically back-scattered ions. Also, Vasco et al.[12] developed a software tool, MORIA, to display metal nanoparticles in cells in a 3D environment using the depth distribution obtained from EBS spectra.

Similar results are not yet available for medium and high Z matrices; however, such a milestone could be reached by performing 3D visualization of the elemental in-depth information obtained after combining data from the PIXE and EBS spectra for each map pixel. The combination of, at least, these two IBA techniques will be essential for having 3D information on medium and high Z matrices as these techniques provide the required complementary information.

This work shows how nonhomogeneous regions, unnoticed or barely distinguishable in the elemental distribution maps obtained by PIXE, can be exposed through the 2D EBS maps obtained at a certain fixed sample depth scale.

Such a possibility is extremely useful in some structures and devices where homogeneity is needed at the surface and in depth for a proper operation. Such an example is the complex semiconductor multilayer structures used in $Cu(In,Ga)Se_2$ (CIGS)-based solar cells, where both lateral and depth variation of composition originate several problems, such as band gap fluctuations, leading to significant open-circuit voltage losses.[13,14] Several authors have determined the in-depth elemental gradient due to Ga and In variations[15–18] or Cu content;[19] however, depending on the manufacturing technique used, artifacts and inconsistencies can still be evaluated when using micrometer-resolved analytical methods. Previous research studies, using a broad ion beam, have demonstrated the suitability of IBA techniques to characterize these type of cells,[8,9,15,16,20,21] obtaining Ga and In depth profiles similar to those obtained by other techniques such as secondary ion mass spectroscopy (SIMS),[22,23] with the advantage of being nondestructive and that do not require any special sample preparation.

According to "Best Research-Cell Efficiency Chart" from NREL,[24] the record efficiency for research cells based on CIGS is 23.4%. CIGS-based solar cells can be easily found in the market, being a competitor of other thin-film technologies based on CdTe or a-Si. Furthermore, CIGS cells are good candidates for the development of tandem solar cells with another emerging technology: perovskite solar cells.[25] Many of the research efforts in this technology are made to control and know the composition of the absorber and buffer layers, but the knowledge of in-depth elemental distribution in finished cells needs further investigation.

Looking for micro-inhomogeneities and composition defects, different CIGS solar cells devices were analyzed by means of IBA techniques in a nuclear microprobe, and the obtained results are presented in this work. In-depth compositional variations were found out; some of them were related to the manufacturing processes, which can act as active electric and optoelectronic defects, being the main culprits for solar cell efficiency limitations. Therefore, expanding the family of techniques that can probe such properties is always looked for by the research community.

2. MATERIALS AND METHODS

EBS and PIXE measurements were performed at normal incidence using an Oxford Microbeams nuclear microprobe.[26] X-rays were detected with a 30 mm² Bruker SDD detector with 145 eV resolution, positioned at 135° with the beam direction at a distance of 20 mm from the sample, while the backscattered particles were detected with a 200 mm² PIPS detector with 30 keV resolution, positioned at 140° scattering angle in Cornell geometry at a distance of 50 mm from the sample. Proton beams were generated from a 2.5 MV single-ended Van de Graaff accelerator.

Solar device structures based on CIGS were prepared as described in ref 22, with the CIGS layer grown using a standard coevaporation process. The EBS and PIXE measurements were performed in finished solar cells; that is, the structure comprises a soda-lime glass (SLG) substrate of 1 mm thickness with a Mo back contact (350 nm), followed by the CIGS absorbing layer (1700 nm), CdS and i-ZnO buffer layers (70 and 90 nm, respectively), the ZnO/Al front contact (350 nm), and contacting metal grids Ni/Al/Ni (100 nm/3000 nm/100 nm), each of them occupying 2.5% of the total area. The thickness values presented are nominal values not reflecting the final thickness values as they vary from solar cell to solar cell depending on the processing conditions and fluctuations in the growth process, as described in ref 22.

For their characterization and with the aim of optimizing the depth-resolved information, 900 keV or 1 MeV (nominal energy) proton beams with about 100 pA beam current were used. With these energy values and considering the thickness mentioned above, the EBS spectra can give information up from the top electrode (ZnO/Al) down to the SLG substrate, being capable of probing the full device. Typical ion beam spatial resolution is 3×4 μm^2.

The OMDAQ software package[27] was used for beam control, data acquisition, and postdata treatment. 2D-PIXE and EBS maps were obtained using the listmode playback mode by selecting the desired regions of interest (ROIs) in each spectrum.

Maps and point PIXE spectra were analyzed using GUPIX[28] software to extract the elemental peak areas that are used as input data in the NDF v9.6a code,[29] which simultaneously fits the PIXE and EBS spectra providing for a self-consistent solution. Thickness values are given in areal density (i.e., atoms/cm²), the standard units in IBA analyses. For guidance, an estimation of the thickness values is presented in nanometer units, considering, for compound densities, the weighted average of the bulk densities. The default uncertainty considered in NDF for PIXE is 10%. NDF fit is done
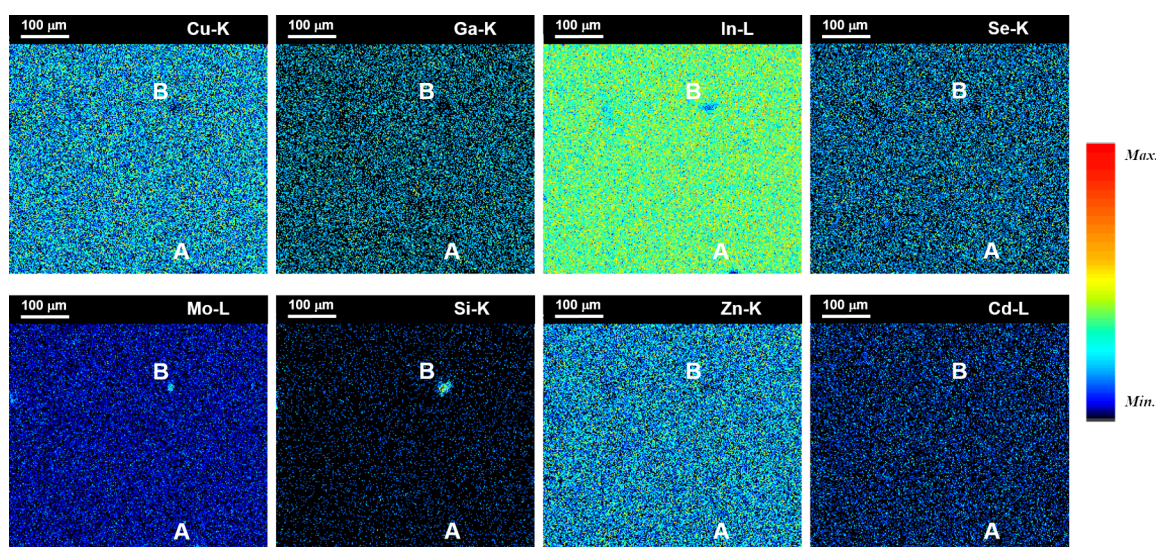
Figure 1. 2D elemental distribution maps ($530 \times 530 \ \mu m^2$) from PIXE spectra (900 keV proton beam) for the elements present in the CIGS absorber layer (Cu, In, Ga, and Se), ZnO, Mo layers, and SLG (Si). Labels A and B are inhomogeneous regions referred in the text.
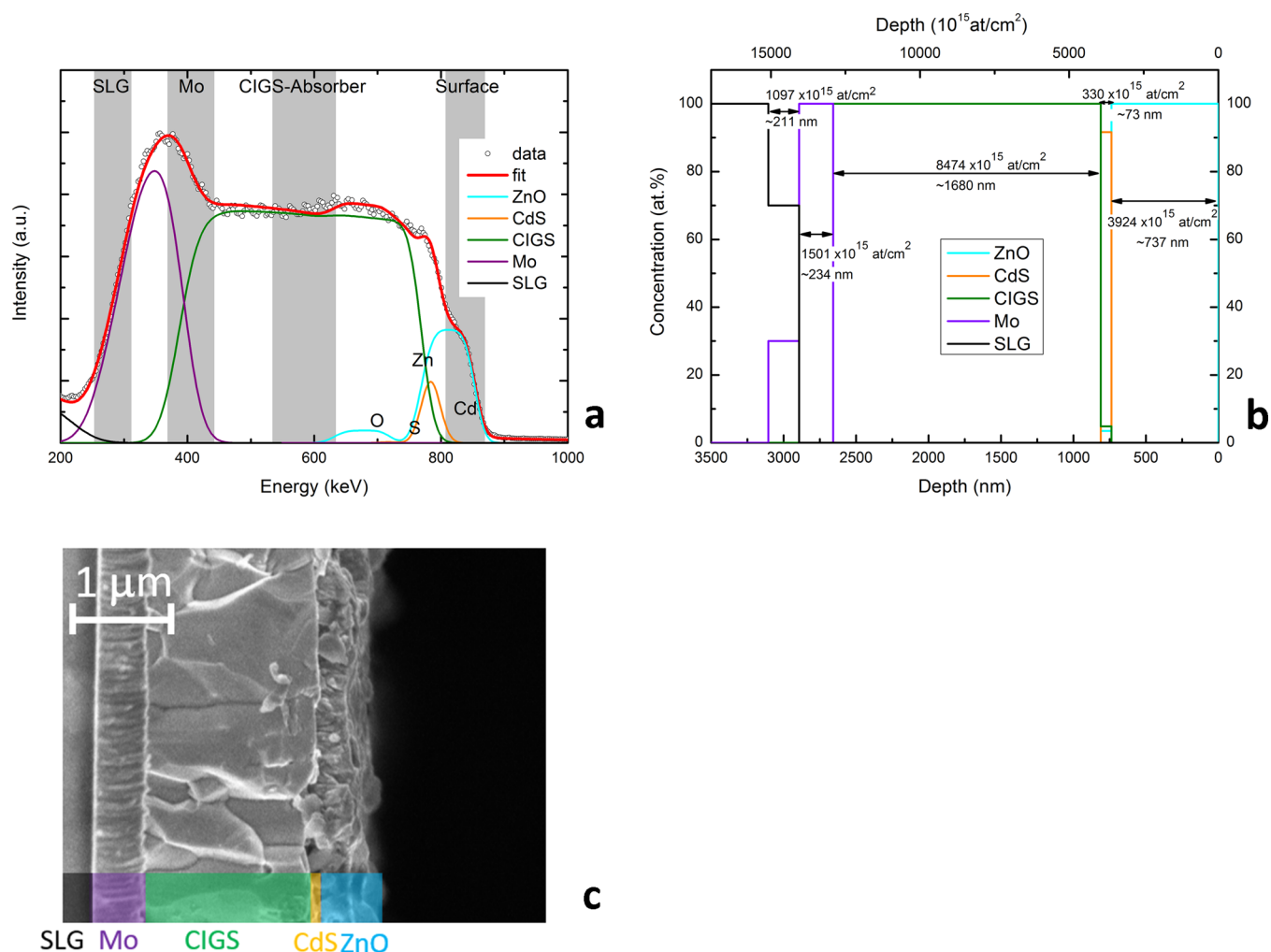

Figure 2. (a) EBS spectrum, fit and partial spectra of the layers and SLG contribution. For reasons of clarity, the CIGS partial spectrum is the sum of the individual Cu, Ga, In, and Ga signal contributions. The spectrum is the one recorded at 900 keV over an area of $530 \times 530 \ \mu m^2$, as shown in Figure 1. Shadowed areas refer the ROIs used to obtain the maps shown in Figure 4. (b) Depth profiles for the different layers obtained from the fit. (c) Cross-sectional SEM image of the CIGS solar cell.
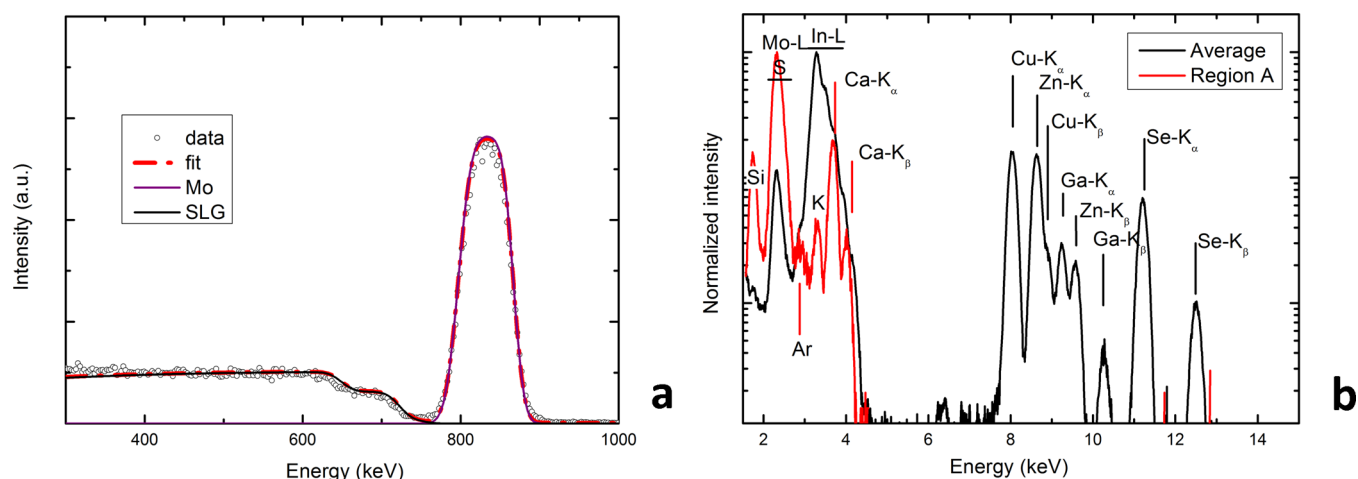
Figure 3. (a) EBS spectrum and fit of region A (see Figure 1). (b) PIXE spectrum from region A; for a better comparison, PIXE spectrum for the average scan has been included.
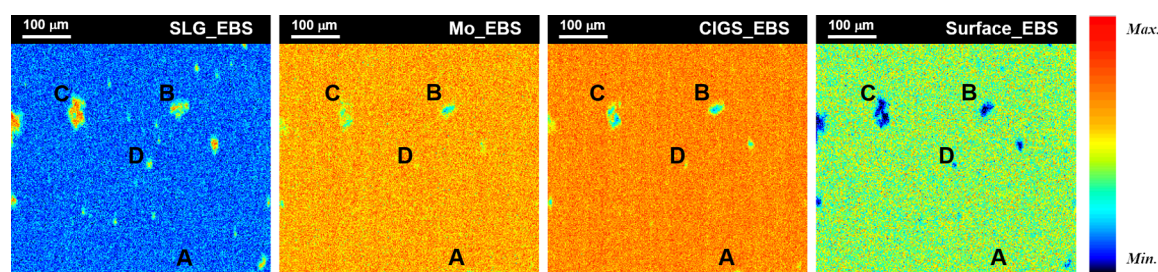

Figure 4. 2D maps ($530 \times 530 \ \mu m^2$) from EBS spectra (900 keV proton beam), considering the ROIs shown in the EBS spectrum (Figure 2a). Labels A, B, C, and D are inhomogeneous regions referred in the text.

minimizing a χ^2 function; a complete analysis of RBS (Rutherford backscattering spectrometry) accuracy can be found in ref 30.

High-resolution cross section images were obtained by scanning electron microscopy (SEM) using a FEI Nova Nano 650 system using acceleration voltages of 3 and 5 kV. The cross sections were achieved by mechanically cleaving the solar cells.[31] This process creates non-uniform cuts, and to counter this, large areas are analyzed; hence, the image presented here is representative of the analyzed area.

3. RESULTS

The 2D-PIXE elemental distribution maps for a CIGS device are shown in Figure 1. There are two regions (A and B) or clusters with a dimension of 20−30 μm with an elemental concentration that varies significantly from the rest of the area under study. These maps were recorded using a 900 keV proton beam over a region of $530 \times 530 \ \mu m^2$. We note that different areas were analyzed, and similar abnormal regions were found throughout the whole sample. In Figure 2a, the average EBS spectrum recorded during the experiment when scanning the entire $530 \times 530 \ \mu m^2$ area is shown. The fit of this EBS spectrum, considering as input data the PIXE concentrations of each element obtained from the average PIXE spectrum, shows a layer of 3924×10^{15} at/cm^2 (~737 nm) of ZnO (oxygen rich) followed by a 330×10^{15} at/cm^2 (~73 nm) of CdS, a CIGS film of about 8474×10^{15} at/cm^2 (~1680 nm), and a 1501×10^{15} at/cm^2 (~234 nm) single layer of molybdenum, which show a spreading toward the SLG of 1097×10^{15} at/cm^2 (211 nm). Notice that although EBS

and PIXE have no sensitivity to chemical bonds, the fitting model of NDF allows defining molecules (instead of elements) with a fixed or variable stoichiometry, the depth range where elements/molecules can exist, and the concentration range in which they can vary. This procedure provides a sounder problem solution while saving computer processing time.[32] In Figure 2a, "ZnO, CdS, CIGS, and SLG" are labelled as compounds: these are treated as "logical elements" by the computation engine of NDF, which thus imposes "chemical priors" onto the data (as discussed by Butler[33]). Individual spectra for Zn, O, Cd, and S are shown in the figure, nevertheless Cu, Ga, In, and Se signals have been replaced by their sum and labelled as "CIGS" for better visualization of the different layers. Same procedure was done for the SLG substrate.

The obtained depth profile, jointly with the concentration values, is shown in Figure 2b. Regarding the CdS layer, the obtained data (90% CdS and 10% ZnO + CIGS) can be explained considering the layer thickness and roughness of the layers observed in Figure 2c. As such, the resulting fit assigns to this layer a small amount of the compounds found in the neighboring layers. Furthermore, the obtained average CIGS composition is $Cu_{0.79}(In_{0.73}Ga_{0.27})Se_{1.72}$ ([Cu]/([Ga] + [In]) ratio is 0.79 and [Ga]/([Ga] + [In]) = 0.27), aligned with the expected values extracted from X-ray fluorescence after the growth process. The estimated thickness and composition values are within margin uncertainties of the expected nominal values.

2D-PIXE maps (Figure 1) show small regions with a high concentration of silicon and molybdenum and a reduced or inexistent signal from the other elements belonging to the
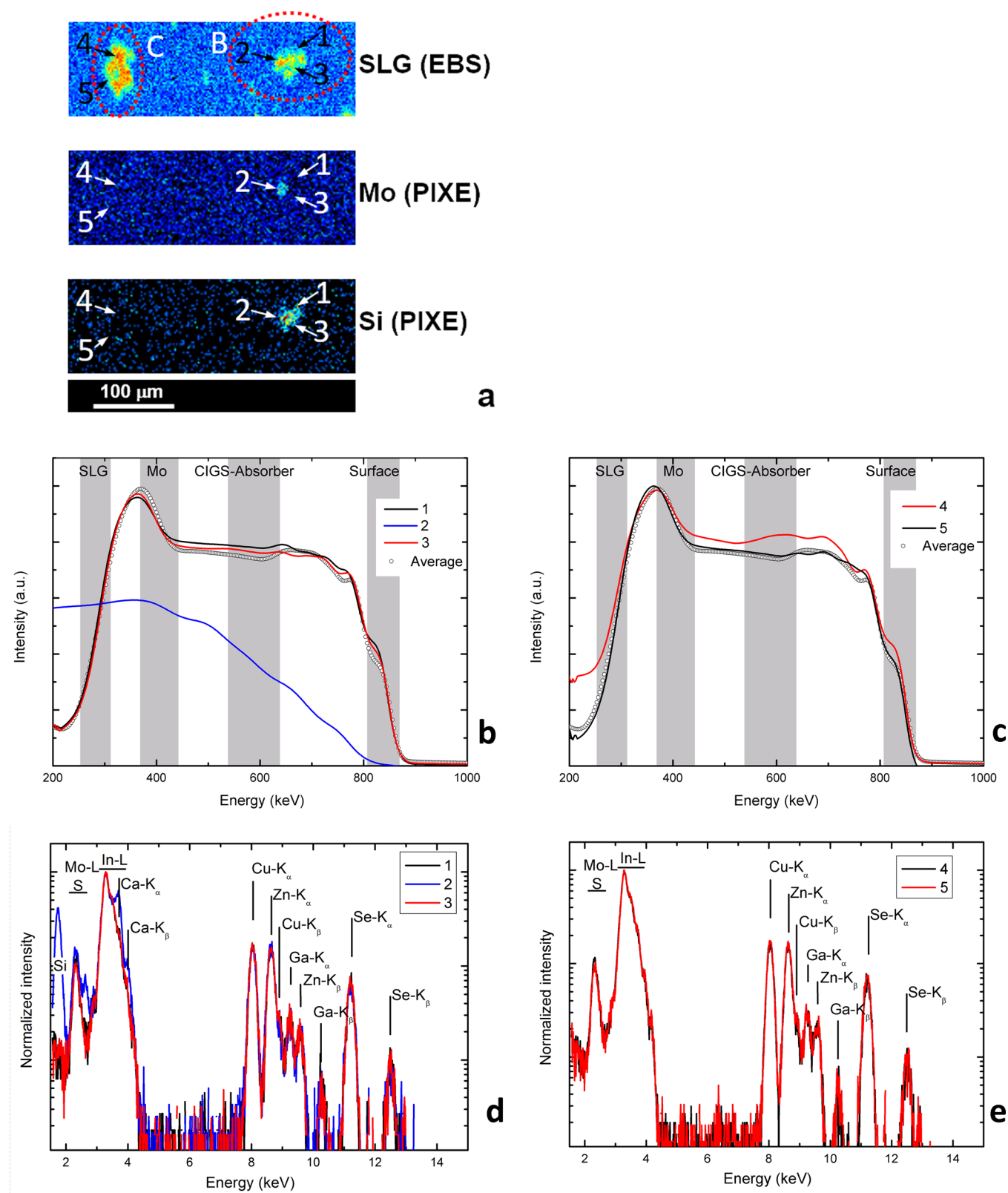
Figure 5. (a) Close view of the 2D maps showing regions B and C (SLG, Mo, and Si) from Figures 1 and 4. Sites of point analyses performed are identified by numbers 1−5. (b−e) EBS (b,c) and PIXE spectra (d,e) for each point.

active CdS and ZnO layers. Regarding region A, visible in almost all 2D-PIXE maps, a point analysis was performed (see Figure 3). This region consists of about 1818×10^{15} at/cm^2 ($\sim$283 nm) of Mo on top of the SLG substrate (see Figure 3a),

where it is also possible to detect a small amount of Argon atoms (1.5 at. %), as can be seen in the PIXE spectrum (Figure 3b), jointly with the other elements from the glass (Ca, K, and Si). Region B in Figure 1 can also be observed in all 2D maps,
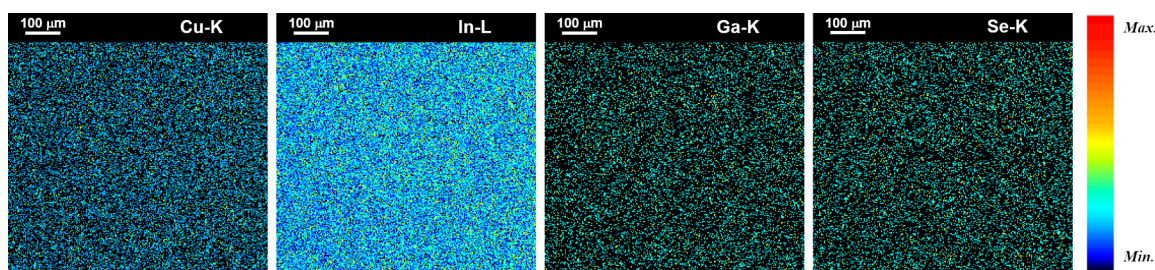
Figure 6. 2D elemental distribution maps ($750 \times 750 \ \mu m^2$) from PIXE spectra (1 MeV proton beam) for the elements present in the CIGS absorber layer: Cu, In, Ga, and Se.
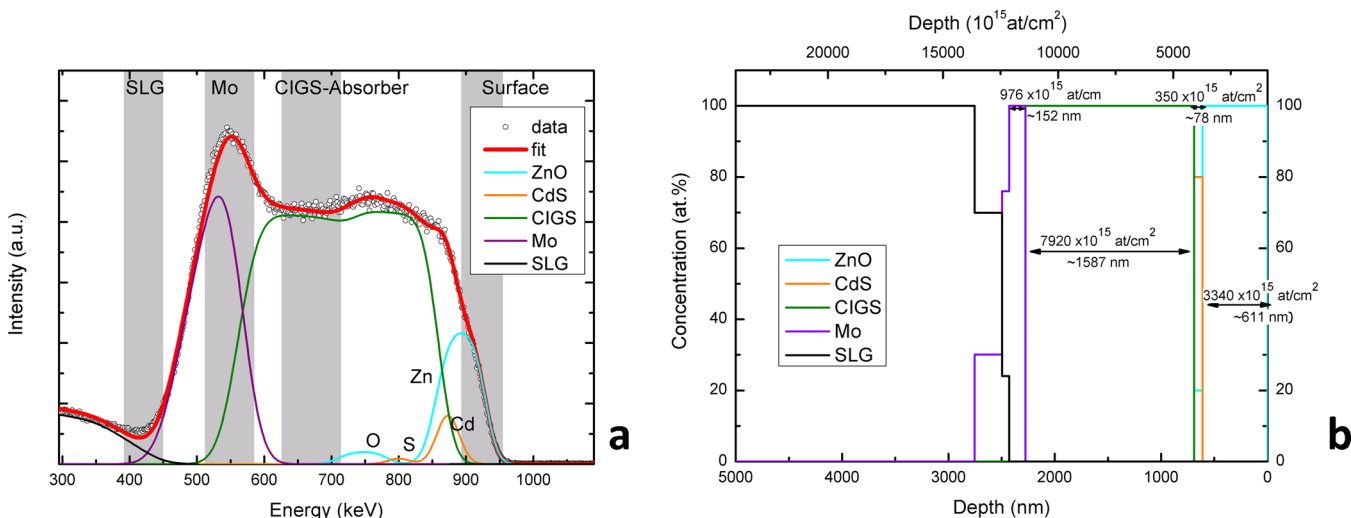

Figure 7. (a) EBS spectrum, fit and partial spectra of the layers and SLG contribution. For reasons of clarity, the CIGS partial spectrum is the sum of the individual Cu, Ga, In, and Ga signals contributions. The spectrum is the one recorded at 1 MeV over an area of $750 \times 750 \ \mu m^2$, as shown in Figure 6. Shadowed areas refer the ROIs used to obtain the maps shown in Figure 8. (b) Depth profiles for the different layers obtained from the fit.

with different dimensions, being larger in the Si map, probably due to the beam straggling effect (as the proton beam penetrates the sample, the slowing down is accompanied by a spread both in space and energy). This region composition will be discussed in detail later.

2D maps can also be obtained from the ROIs selected in the average EBS spectrum (shown in Figure 2a in gray color). The maps obtained from these ROIs are shown in Figure 4, which have been labeled (according to the average EBS spectrum) as surface, CIGS-absorber layer, Mo contact, and SLG. Nevertheless, although EBS provides information about the elemental depth profile, the inhomogeneities detected in the maps cannot be straightforward related to these layers.

In these 2D-EBS maps, inhomogeneous regions can be found; some of them are visible in all maps and others only in some of them. Furthermore, previous mentioned regions (A and B) are clearly observed in the 2D-EBS maps, but new regions (C and D) are not visible, or barely distinguishable, in any of the PIXE maps (Figure 1). These heterogeneities were found to be related to both the layer thickness and composition irregularities.

A close view of regions B and C is shown in Figure 5a, and a detailed observation of the elemental distribution in these regions was made. Five-point analyses (within the system resolution) were performed, labelled as 1, 2, 3, 4, and 5; EBS and PIXE spectra obtained on these points are shown in Figure 5b−e, where, for a better comparison, the average EBS fitted spectrum (Figure 2a) has been included.

Region B can be related to a SLG substrate irregularity (point 2), considering the results from the EBS and PIXE spectra. PIXE spectrum shows as main peaks those associated with Si and Ca (from SLG), and also peaks from the other elements of the cell are observed. Furthermore, the corresponding EBS signal starts at about 820 keV, which is compatible with the presence of glass at the surface. Around this point 2, it seems that the CIGS film grew normally with a uniform thickness, similar to that obtained for the entire map.

Considering the EBS signals, the inhomogeneities of region B (points 1 and 3) are related to thickness variations of the top layers containing Zn and Cd. According to the EBS fit, the CdS and ZnO layers (surface layers) are thicker for point 3 than for point 1 [4691×10^{15} at/cm^2 ($\sim$890 nm) and 4365×10^{15} at/cm^2 ($\sim$825 nm), respectively], both being slightly larger than the average value [4254×10^{15} at/cm^2 ($\sim$810 nm)]. Regarding the CIGS layer, although the thickness value is almost the same, the concentration of Se and In is slightly higher than that obtained for the average region, increasing thus the individual contributions to the EBS spectra.

In region C, no signal from the SLG substrate was detected by PIXE. Points 4 and 5 have similar thickness values for CdS and ZnO layers, being also similar to that obtained for the average region. Nevertheless, point 4 exhibits higher Zn concentration (about 60 at. %) than point 5 (50 at. % of Zn). Concerning the active CIGS layer, in both points, the thickness and composition values are quite close to that obtained for the average map. However, the Mo signal is wider, particularly for
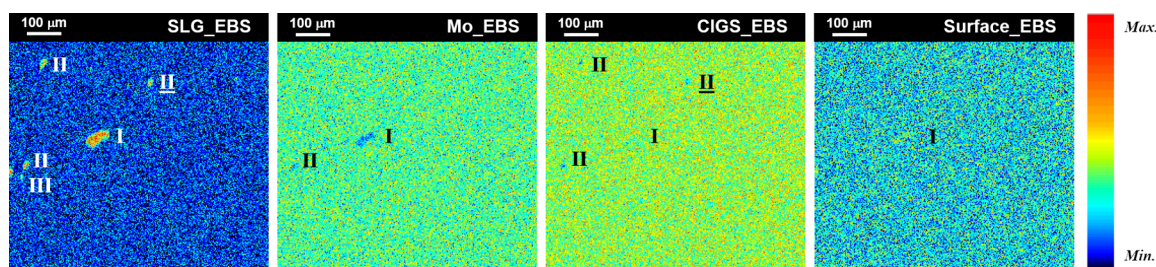
Figure 8. 2D maps ($750 \times 750 \ \mu m^2$) from EBS spectra (1 MeV proton beam), considering the ROIs shown in the EBS spectrum (Figure 7). Labels I, II, and III are inhomogeneous regions referred in the text.
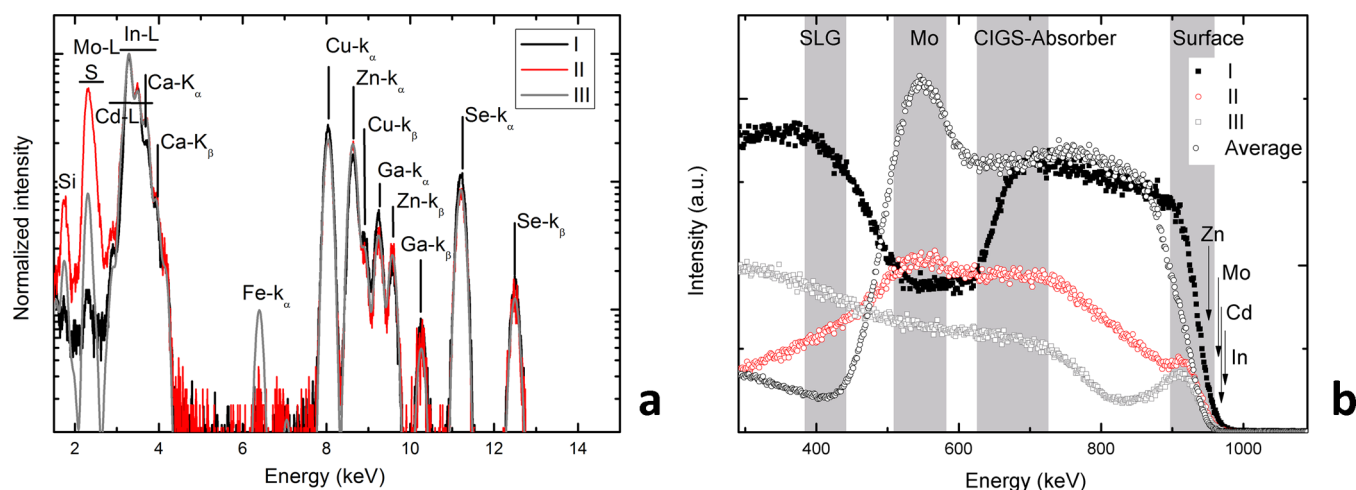

Figure 9. Point PIXE (a) and EBS (b) spectra (1 MeV proton beam) recorded in points I, II, (underlined) and III (see Figure 8). In the EBS spectrum, the surface barrier positions for Zn, Mo, Cd, and In are labeled.

point 4, then contributing to the higher intensity signal and contrast observed in Figure 5a for the SLG ROI. This indicates glass surface microscale irregularities and the corresponding variation of the deposited Mo layer.

Analogous information can be extracted from the analysis of other CIGS solar cells. Figure 6 shows the elemental distribution maps ($750 \times 750 \ \mu m^2$) obtained from PIXE spectra of the absorber layer constituents (Cu, In, Ga, and Se) from another CIGS device. The maps indicate a homogeneous distribution for all elements present in the cell within the system resolution. Figure 7a shows the corresponding average EBS spectrum recorded during the experiment and the fit, considering as input data the concentrations of each element obtained by GUPIX. As shown in Figure 7b, the best fit consists of a 3340×10^{15} at/cm^2 (~611 nm) film of ZnO, followed by a 350×10^{15} at/cm^2 (~78 nm) layer of ZnO and CdS (with composition of 20 and 80 at. % respectively), then a CIGS film of about 7920×10^{15} at/cm^2 (~1587 nm), and a single Mo layer of 976×10^{15} at/cm^2 (~152 nm) thick. This layer shows also a 1700×10^{15} at/cm^2 (~324 nm) mixed layer related to substrate roughness. Furthermore, the composition obtained for this layer is $Cu_{0.93}(In_{0.71}Ga_{0.29})Se_{1.92}$ ($[Cu]/([Ga] + [In]) = 0.93$ and $[Ga]/([Ga] + [In]) = 0.29$). Equivalent results for both composition and thicknesses were obtained in points randomly selected in the 2D-PIXE maps.

Figure 8 shows the 2D-EBS maps obtained from the ROIs defined in Figure 7a, as previously discussed. In these EBS maps, inhomogeneous regions can be found, some of which are visible in all maps (labelled as I), others in some maps (II), and others in only one of them (III) and barely distinguishable in

any of the PIXE maps (Figure 6). These heterogeneities are related to both thickness and composition irregularities as it can be observed in Figure 9, where PIXE and EBS spectra recorded on points I, II (underlined in Figure 8), and III are shown.

Considering the PIXE spectra, the main differences are found in the low-energy region, where peaks related to Si and Ca (from the SLG substrate) are much higher for points II and III than for point I. Also, in those two points, the signal at 2.3 keV is higher than for point I, which could be related to variations in the thickness of the CdS or Mo layers, most likely to the Mo layer once variation in the Cd signal is not noticed. On the other hand, point I shows a peak with low intensity at 2.3 keV, while the intensities of peaks related to Se, Ga, and Cu are slightly higher than in the other points.

For each analyzed point, diverse compositional profiles can be obtained, all of them quite different from the average EBS spectrum (Figure 7) and from the previous analyzed CIGS cell. A small shift toward high energy is detected for point I, which could be associated with the presence at the surface of elements with atomic number higher than Zn ($K = 0.94700$) but, as shown in Figure 7, lower than Cd ($K = 0.96883$) or In ($K = 0.96947$) as for the case of Mo ($K = 0.96358$), K being the kinematic factor, the energy ratio of the projectile particle and of the scattered particle.[34] However, the Mo signal in the PIXE spectra for point I is very weak, and hence its presence at the surface can be excluded. Then, the shift can be explained considering a thin layer of ZnO (about 92 nm instead of the ~600 nm average value), resulting in the shift of the Cd signal towards higher energies. This means that due to a surface
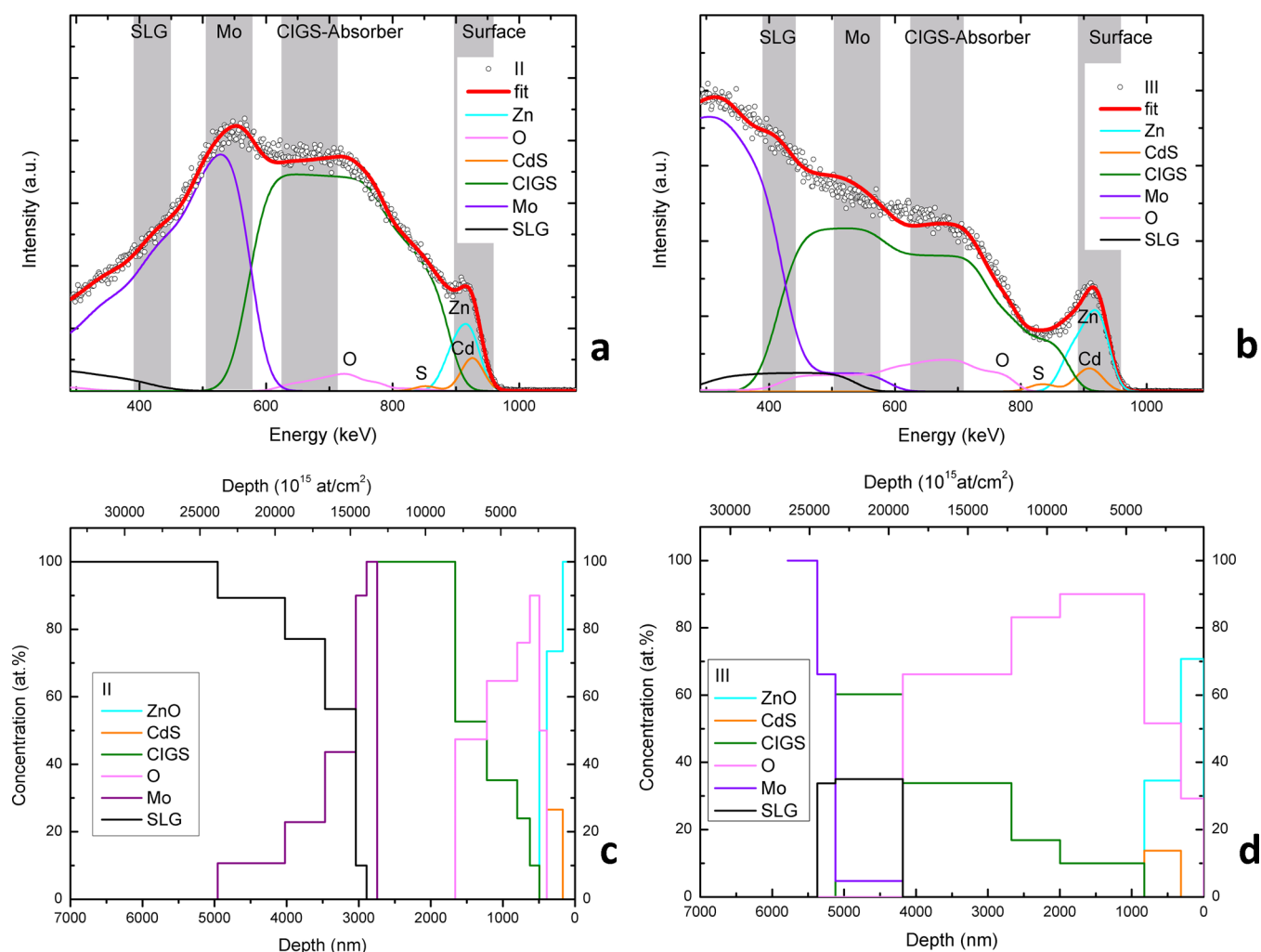
Figure 10. EBS spectra, fit and partial spectra of each layer: (a) point II; (b) point III. (c) Depth profile for point II; (d) depth profile for point III.

defect in that area, probably produced during the growth process, the needed thickness of ZnO layer was not achieved. The evolution of the signal in-depth (drop and rise between energies 500 and 700 keV) was not possible to determine, and more data are needed to explain this behavior.

In Figure 10 the proposed fits of EBS spectra for points II and III are shown. Both are characterized by a clear signal from the upper layers, followed by the CIGS film. In both points, an extra contribution of oxygen content had to be assumed in order to obtain a proper fit. Point II shows a Mo profile further extending into the SLG substrate than the one observed for the average spectrum map, while for point III, the Mo layer seems to be thicker.

4. DISCUSSION

The use of a nuclear microprobe, where it is possible to focus and raster the particle beam, and the simultaneous acquisition of PIXE and EBS spectra allow one to visualize not only the elemental distribution over the surface (with micrometer spatial resolution) but also the elemental in-depth variations on CIGS solar cells (with resolution down to the nanometer range, depending on the species and energy of the ion beam used and layer composition). Also, by combining multiple IBA spectra and using the NDF code, it was possible to obtain the

composition and depth profile in different scenarios, allowing both quantitative and qualitative analyses.

Figure 3 shows a trivial defect where data from PIXE (showing the presence of Ar) were very important to unambiguously correlate this defect and the manufacturing process. Argon is used as the ionization gas during the sputtering processes of the Mo layer and the front contact.[22] Hence, it is likely that in region A (in Figure 1), CIGS has peeled off and it is now acting as an electrical shunt and/or a dead region, both cases being very detrimental for the solar cell performance.

Figures 4 and 5 show the importance of the qualitative results obtained, which correspond to heterogeneous regions revealed when using the 2D maps from EBS spectra. Those regions are related to small differences in the layer thickness when compared with the average results. Too thick CdS and ZnO layers (see points 1 and 3 in Figure 5) will increase the device series resistance leading to poor fill factor values, and these nonuniformities should be avoided. The presence of glass at the micrometer scale (see point 2 in Figure 5) could be related to sample manipulation damage such as scribing for cell definition or to the growth conditions, which at this region were not met for a favorable growth of the layers.

On the other hand, EBS spectra (Figures 9 and 10) recorded in defects shown in Figure 8 are hard to fit. To obtain a fit

consistent with the data, the presence of free oxygen was considered, although as Butler[33] pointed out, there may be two or more different solutions that provide equally good fits of simulated spectrum to experimental spectrum. To overcome the ambiguity, as Jeynes et al. showed in ref 35 there are two approaches to constrain the solutions found: collect multiple spectra and/or use restrict conditions in the structure based on previous knowledge of the sample. Unfortunately, from PIXE, the presence of oxygen cannot be confirmed, although the concentration of the visible elements acts as restrict condition. It is also known that prior to the deposition of the buffer layer, the samples are in open air for about 5 min. During this period, oxidation and other reactions of the CIGS surface start to occur due to both oxygen and water in ambient air.[36]

The proposed solution can be considered unsuitable, and it is more appropriate to consider the possible chemical bindings to obtain a more reliable composition (this possibility is easily accepted by the NDF code). Nevertheless, the mechanisms and recombination kinetics that may occur in the CIGS/CdS interface are very dependent on the oxygen exposure; examples are Cu and Cd interdiffusion or the formation of SeO_2, $CdCuS$, and Cu_2Se compounds, among others.[36-40] Because of that, to obtain a reliable solution for these EBS spectra, considering the presence of different compounds, more information is needed, which can be obtained by other analytical techniques.

Generally speaking, several types of defects can be found in CIGS solar cells by means of IBA techniques. We have identified several defects that contribute to lower the overall optoelectronic performance, demonstrated by the illuminated $J-V$ figures of merit of solar cells: (i) dead areas, that is, CIGS regions that are not electrically active; hence there is no extraction of photo-generated current, contributing to smaller values of short-circuit current density when compared with active areas; (ii) nonuniform thicknesses of CdS and the window layers that can lead to variations in the charge extraction resistance, lowering the fill factor; and (iii) variations in the composition of the CIGS layer itself that can lead to the creation of secondary phases, energy band gap variations, or recombination channels, increasing the number of active defects and hence lowering the open-circuit voltage.

Most of these defects might be related to the thickness of the different layers involved. This fact is connected to the manufacturing methods (chemical bath deposition for CdS buffer layer and sputtering for front contacts) or to the glass irregularities. It is known that when using chemical bath deposition, in certain cases, nucleation points lead to agglomerates of colloids preformed in the solution reacting with the surface and leading to thick regions in those places. With regards to sputtering, this technique is also not fully conformal as regions with different aspect ratios can lead to shadowing or other geometrical effects resulting in quite different thicknesses. In what accounts for the glass irregularities, they play an important role during the nucleation phase, and the upper layers will inherit these imperfections during growth.

Another important issue to be highlighted is the time needed to obtain the results, including also the machine time. To acquire maps with an acceptable counting statistics, about 1 h is needed. If nonhomogeneous regions are found within this period, then point analysis can take about 10 min. However, if the maps are being processed later using the listmode playback mode (as partially done in this work), longer runs are needed to ensure a good counting statistics in each pixel of the map. However, the playback mode allows obtaining further and more detailed results in off-line conditions without further need of machine time.

There are many studies about elemental distribution using, for example, electron microscopy techniques, where cross sections are specifically prepared. When using electrons to probe samples, the penetration depth of the electrons is very low when compared with protons. The use of MeV ion beams allows imaging on finished cells in a nondestructive way, without the need of any preparation.

5. CONCLUSIONS

The suitability of using low-energy proton beams (~1 MeV) for the IBA characterization of the complex thin layer structures of CIGS solar cells is shown. By combining 2D maps obtained from PIXE and EBS spectra recorded in different regions of the studied solar cells, we demonstrated the in-depth detection of nonhomogeneous regions. Such identification could not be done when considering only the 2D elemental distribution maps reconstructed from the PIXE spectra.

Knowing the in-depth compositional variations in the CIGS structures is of utmost importance as they are most certainly related to recombination centers, shunt-paths, dead areas, and so forth, which affect the overall solar cell performance. We have identified three types of defects: (i) dead areas, (ii) charge extraction variations in the buffer and transparent conductive oxide layers, and (iii) different CIGS compositions that can lead to modification in the active recombination channels. The identification of these problems through ion beam analysis is important as typically these issues are hard to pinpoint using only one technique.

The procedure presented in this work can be applied to other materials and devices using nuclear microprobe spectroscopy, and it allows studying final devices in a nondestructive way. This work also shows that recording multiple spectra is fundamental for extracting as much information as possible, allowing both quantitative and qualitative results. Furthermore, a good knowledge of the techniques and related analysis codes is fundamental for data interpretation. The variations now detected at certain depths in the EBS maps were found to be both due to layer overlap and signal shifts resulting from composition or thickness variation. For each singularity found, a detailed analysis was performed to ensure a self-consistent analysis. Finally, the obtained results allow considering that it will be possible to get general in-depth 2D map slices to perform a 3D image reconstruction, as already done for low Z matrix containing small quantities of heavy atoms. Although the procedure for the reconstruction of the 3D maps will require long measurement periods and data processing times, they can be shortened with, for example, the use of neural networks trained for each solar cell structure.

■ AUTHOR INFORMATION

Corresponding Author

Victoria Corregidor − *C2TN, Campus Tecnológico e Nuclear, Instituto Superior Técnico, Universidade de Lisboa, Sacavém 2686-953, Portugal; IPFN, Instituto Superior Técnico, Universidade de Lisboa, Lisboa 1049-001, Portugal;* ⓞ orcid.org/0000-0001-8323-0634; Phone: +351 21 994 6080; Email: vicky.corregidor@ctn.tecnico.ulisboa.pt; Fax: + 351 21 994 6285

Authors

M. Alexandra Barreiros − *Laboratório Nacional de Energia e Geologia, UME, Lisboa 1649-038, Portugal*

Pedro M. P. Salomé − *International Iberian Nanotechnology Laboratory, Braga 4715-330, Portugal; Departamento de Física, Universidade de Aveiro, Aveiro 3810-193, Portugal*

Luís C. Alves − *C2TN, Campus Tecnológico e Nuclear, Instituto Superior Técnico, Universidade de Lisboa, Sacavém 2686-953, Portugal*

Complete contact information is available at:
https://pubs.acs.org/10.1021/acs.jpcc.1c02731

Author Contributions

V.C., L.C.A., and M.A.B.—IBA experimental concept and optimization of the analysis parameters and experimental procedure; V.C.— data fit and interpretation and original draft preparation; M.A.B. and L.C.A.—definition of problems to solve, assistance in data fitting, and results coherence; P.M.P.S.—fabrication of the cells under analysis, SEM data analysis, and interpretation of data results versus electrical and optical properties. The final manuscript version was written and reviewed with contributions from all authors. All authors have given approval to the final version of the manuscript.

Notes

The authors declare no competing financial interest.

■ REFERENCES

(1) Jeynes, C.; Colaux, J. L. Thin Film Depth Profiling by Ion Beam Analysis. *Analyst* **2016**, *141*, 5944−5985.

(2) Grime, G. W.; Zeldin, O. B.; Snell, M. E.; Lowe, E. D.; Hunt, J. F.; Montelione, G. T.; Tong, L.; Snell, E. H.; Garman, E. F. High-Throughput PIXE as an Essential Quantitative Assay for Accurate Metalloprotein Structural Analysis: Development and Application. *J. Am. Chem. Soc.* **2020**, *142*, 185−197.

(3) Šmit, Ž. Physics Beyond PIXE. *Nucl. Instrum. Methods Phys. Res., Sect. B* **2020**, *477*, 13−18.

(4) Jeynes, C.; Palitsin, V. V.; Kokkoris, M.; Hamilton, A.; Grime, G. W. On the Accuracy of Total-IBA. *Nucl. Instrum. Methods Phys. Res., Sect. B* **2020**, *465*, 85−100.

(5) Breese, M. B.; Jamieson, D. N.; King, P. J. *Materials Analysis Using a Nuclear Microprobe*; Wiley VCH: Sussex, 1996.

(6) Jallot, E.; Lao, J.; John, Ł.; Soulié, J.; Moretto, P.; Nedelec, J. M. Imaging Physicochemical Reactions Occurring at the Pore Surface in Binary Bioactive Glass Foams by Micro Ion Beam Analysis. *ACS Appl. Mater. Interfaces* **2010**, *2*, 1737−1742.

(7) Watt, F.; Chen, X.; Vera, A. B. D.; Udalagama, C. N. B.; Ren, M.; Kan, J. A. v.; Bettiol, A. A. The Singapore High Resolution Single Cell Imaging Facility. *Nucl. Instrum. Methods Phys. Res., Sect. B* **2011**, *269*, 2168−2174.

(8) Barreiros, M. A.; Alves, L. C.; Brites, M. J.; Corregidor, V. Depth Profile by Total IBA in Perovskite Active Layers for Solar Cells. *Nucl. Instrum. Methods Phys. Res., Sect. B* **2017**, *404*, 211−218.

(9) Brites, M. J.; Barreiros, M. A.; Corregidor, V.; Alves, L. C.; Pinto, J.; Fortunato, E.; Martins, R.; Mascarenhas, J.; Mascarenhas, J. Ultrafast Low-Temperature Crystallization of Solar Cell Graded Formamidinium-Cesium Mixed-Cation Lead Mixed-Halide Perovskites Using a Reproducible Microwave-Based Process. *ACS Appl. Energy Mater.* **2019**, *2*, 1844−1853.

(10) Soulié, J.; Hardy-Dessources, A.; Nedelec, J.-M.; Jallot, E. 3d Organized Macroporous Bioactive Glasses: A Study of Pore Size Effect on Physicochemical Reactivity by Micro-PIXE-RBS. *J. Phys. Chem. C* **2013**, *117*, 6702−6711.

(11) Chen, X.; Chen, C.-B.; Udalagama, C. N. B.; Ren, M.; Fong, K. E.; Yung, L. Y. L.; Giorgia, P.; Bettiol, A. A.; Watt, F. High-Resolution 3D Imaging and Quantification of Gold Nanoparticles in a Whole Cell Using Scanning Transmission Ion Microscopy. *Biophys. J.* **2013**, *104*, 1419−1425.

(12) Vasco, M. S.; Alves, L. C.; Corregidor, D.; Godinho, C. P.; Sá-Correia, I.; Bettiol, A.; Watt, F.; Pinheiro, T. 3D Map Distribution of Metallic Nanoparticles in Whole Cells Using MeV Ion Microscopy. *J. Microsc.* **2017**, *267*, 227−236.

(13) Rau, U.; Werner, J. H. Radiative Efficiency Limits of Solar Cells with Lateral Band-Gap Fluctuations. *Appl. Phys. Lett.* **2004**, *84*, 3735−3737.

(14) Ghorbani, T.; Zahedifar, M.; Moradi, M.; Ghanbari, E. Influence of Affinity, Band Gap and Ambient Temperature on the Efficiency of CIGS Solar Cells. *Optik* **2020**, *223*, 165541.

(15) Abou-Ras, D.; et al. Comprehensive Comparison of Various Techniques for the Analysis of Elemental Distributions in Thin Films. *Microsc. Microanal.* **2011**, *17*, 728−751.

(16) Karydas, A. G.; Bogdanovic Radovic, I.; Streeck, C.; Kaufmann, C.; Caballero, R.; Rissom, T.; Kanngießer, B.; Beckhoff, B.; Jaksic, M.; Barradas, N. P. In-Depth Elemental Characterization of Cu(In,Ga)-Se2 Thin Film Solar Cells by Means of RBS and PIXE Techniques. *Nucl. Instrum. Methods Phys. Res., Sect. B* **2014**, *331*, 93−95.

(17) Kim, Y. I.; Kim, K. B.; Kim, M. Characterization of Lattice Parameters Gradient of Cu(In1-XGax)Se2 Absorbing Layer in Thin-Film Solar Cell by Glancing Incidence X-Ray Diffraction Technique. *J. Mater. Sci. Technol.* **2020**, *51*, 193.

(18) Iatosti, C.; Moret, M.; Tiberj, A.; Briot, O. Analysis of the Gallium Gradient in Cu(In1-XGax)Se2 Absorbers by X-Ray Diffraction. *Sol. Energy Mater. Sol. Cells* **2021**, *220*, 110847.

(19) Kong, Y.; Huang, L.; Chi, Z.; Wu, X.; Li, J.; Xiao, X. Failure and Recovery Modes of Submicron Cu(In,Ga)Se2 Solar Cells with High Cu Content. *ACS Appl. Mater. Interfaces* **2020**, *12*, 52857−52863.

(20) Karydas, A. G.; Streeck, C.; Radovic, I. B.; Kaufmann, C.; Rissom, T.; Beckhoff, B.; Jaksic, M.; Barradas, N. P. Ion Beam Analysis of Cu(In,Ga)Se2 Thin Film Solar Cells. *Appl. Surf. Sci.* **2015**, *356*, 631−638.

(21) Jeynes, C.; Zoppi, G.; Forbes, I.; Bailey, M. J.; Peng, N. In Characterisation of Thin Film Chalcogenide PV Materials Using MeV Ion Beam Analysis. *2009 International Conference on Sustainable Power Generation and Supply*, 2009; pp 1−6.

(22) Lindahl, J.; Zimmermann, U.; Szaniawski, P.; Torndahl, T.; Hultqvist, A.; Salomé, P.; Platzer-Björkman, C.; Edoff, M. Inline Cu(In,Ga)Se2 Co-Evaporation for High-Efficiency Solar Cells and Modules. *IEEE J. Photovolt.* **2013**, *3*, 1100−1105.

(23) Jang, Y. J.; Lee, J.; Lee, K. B.; Kim, D.; Lee, Y. Quantitative Analysis and Band Gap Determination for CIGS Absorber Layers Using Surface Techniques. *J. Anal. Methods Chem.* **2018**, *2018*, 6751964.

(24) NREL Best Research-Cell Efficiency Chart, https://www.nrel.gov/pv/cell-efficiency.html (accessed June, 2021).

(25) Li, H.; Zhang, W. Perovskite Tandem Solar Cells: From Fundamentals to Commercial Deployment. *Chem. Rev.* **2020**, *120*, 9835−9950.

(26) Alves, L. C.; Breese, M. B. H.; Alves, E.; Paúl, A.; da Silva, M. R.; da Silva, M. F.; Soares, J. C. Micron-Scale Analysis of SiC/SiCf Composites Using the New Lisbon Nuclear Microprobe. *Nucl. Instrum. Methods Phys. Res., Sect. B* **2000**, *161−163*, 334−338.

(27) Grime, G. W.; Dawson, M. Recent Developments in Data Acquisition and Processing on the Oxford Scanning Proton

Microprobe. *Nucl. Instrum. Methods Phys. Res., Sect. B* **1995**, *104*, 107−113.

(28) Campbell, J. L.; Boyd, N. I.; Grassi, N.; Bonnick, P.; Maxwell, J. A. The Guelph PIXE Software Package IV. *Nucl. Instrum. Methods Phys. Res., Sect. B* **2010**, *268*, 3356−3363.

(29) Jeynes, C.; Palitsin, V. V.; Grime, G. W.; Pascual-Izarra, C.; Taborda, A.; Reis, M. A.; Barradas, N. P. External Beam Total-IBA Using Data Furnace. *Nucl. Instrum. Methods Phys. Res., Sect. B* **2020**, *481*, 47−61.

(30) Jeynes, C.; Barradas, N. P.; Szilágyi, E. Accurate Determination of Quantity of Material in Thin Films by Rutherford Backscattering Spectrometry. *Anal. Chem.* **2012**, *84*, 6061−6069.

(31) Salomé, P.; Fjällström, V.; Hultqvist, A.; Edoff, M. Na Doping of Cigs Solar Cells Using Low Sodium-Doped Mo Layer. *IEEE J. Photovolt.* **2013**, *3*, 509−513.

(32) Jeynes, C.; Barradas, N. P.; Rafla-Yuan, H.; Hichwa, B. P.; Close, R. Accurate Depth Profiling of Complex Optical Coatings. *Surf. Interface Anal.* **2000**, *30*, 237−242.

(33) Butler, J. W. Criteria for Validity of Rutherford Scatter Analyses. *Nucl. Instrum. Methods Phys. Res., Sect. B* **1990**, *45*, 160−165.

(34) Chu, W. K.; Meyer, J. W.; Nicolet, M. A. *Backscattering Spectrometry*; Academic Press Inc.: London, 1978.

(35) Jeynes, C.; Barradas, N. P.; Marriott, P. K.; Boudreault, G.; Jenkin, M.; Wendler, E.; Webb, R. P. Elemental Thin Film Depth Profiles by Ion Beam Analysis Using Simulated Annealing - a New Tool. *J. Phys. D: Appl. Phys.* **2003**, *36*, R97−R126.

(36) Metzger, W. K.; Repins, I. L.; Romero, M.; Dippo, P.; Contreras, M.; Noufi, R.; Levi, D. Recombination Kinetics and Stability in Polycrystalline Cu(In,Ga)Se2 Solar Cells. *Thin Solid Films* **2009**, *517*, 2360−2364.

(37) Abou-Ras, D.; Kostorz, G.; Romeo, A.; Rudmann, D.; Tiwari, A. N. Structural and Chemical Investigations of CBD- and PVD-CdS Buffer Layers and Interfaces in Cu(In,Ga)Se2-Based Thin Film Solar Cells. *Thin Solid Films* **2005**, *480−481*, 118−123.

(38) He, X.; et al. The Role of Oxygen Doping on Elemental Intermixing at the PVD-CdS/Cu (InGa)Se2 Heterojunction. *Prog. Photovoltaics Res. Appl.* **2019**, *27*, 255−263.

(39) Mufti, N.; Amrillah, T.; Taufiq, A.; Sunaryono; Aripriharta; Diantoro, M.; Zulhadjri; Nur, H. Review of CIGS-Based Solar Cells Manufacturing by Structural Engineering. *Sol. Energy* **2020**, *207*, 1146−1157.

(40) Regesch, D.; Gütay, L.; Larsen, J. K.; Deprédurand, V.; Tanaka, D.; Aida, Y.; Siebentritt, S. Degradation and Passivation of CuInSe2. *Appl. Phys. Lett.* **2012**, *101*, 112108.